Testing coalescence and statistical-thermal production scenarios for (anti-)(hyper-)nuclei and exotic QCD objects at LHC energies with recent and future experimental data

F. Bellini and A. Kalweit

16th of May 2018

(Anti-)(hyper-)nuclei are unique probes of the medium created in proton-proton, proton-Pb, and Pb–Pb collisions at LHC energies. At LHC energies, their production is typically discussed within the framework of coalescence and thermal-statistical production models. While it is often argued that both approaches are not distinguishable, we present a detailed study of both theories which reveals largely different predictions between the two approach for the production of ^{3}He and hyper-tritons. Confronting our results with recent ALICE measurements, the coalescence approach is found to provide a correct description of the data only in small systems such as pp collisions, while it fails for central Pb–Pb collisions. The thermal-statistical model on the other hand is in agreement with results in central Pb–Pb collisions even though such fragile objects should be destroyed in hadronic interactions after the chemical freeze-out of the system. Our findings thus indicate the existence of a novel production mechanism for these objects and highlight the unique potential of ultra-relativistic heavy-ion collisions as a laboratory to clarify the internal structure of exotic QCD objects.

Contents

1. Introduction

The formation of light anti- and hyper-nuclei in high energy proton-proton (pp), proton-nucleus (pA) and nucleus-nucleus (AA) collisions provides unique observables for the study of the system created in these collisions. In addition, these studies might shed light on the internal structure of the formed objects themselves. In this context, nuclei and hyper-nuclei are special objects with respect to non-composite hadrons (such as pions, protons, kaons, etc.), because their size (i.e. the extension of their wave-function) is comparable to a fraction or the whole system created in the collision [1]. The relevant known properties of the objects under study here are summarised in Table 1. As quantum-mechanical objects, their size is typically defined as the rms of their (charge) wave function, which corresponds to about 2 fm for light (anti-)nuclei as obtained from electron scattering experiments. Not much is known experimentally about the wave-functions of hyper-nuclei and other exotic QCD objects. Theoretical calculations indicate a rms of the wave-function of the hyper-triton of about 5 fm which is significantly larger than that of non-strange $A = 3$ nuclei. This is driven by the average separation of the Lambda with respect to the two other nucleons which is expected to amount up to 10 fm. In principle, halo nuclei as ^{6}He would therefore be ideal for such studies, but they remain out of the experimental reach in high-energy experiments in the near future.

Surprisingly, thermal-statistical models have been successful in describing not only light-flavour particle production, but also that of light (anti-)(hyper-)nuclei across a wide range of energies in nucleus-nucleus collisions [2, 3]. In this approach, particles are produced from a fireball in thermal and kinetic equilibrium with temperatures of the order of $T_{chem} = 156$ MeV (near the temperature of the QCD phase transition boundary, as predicted by lattice QCD calculations [4]). Particle abundances are fixed at chemical freeze-out, when inelastic collisions cease. Further elastic and pseudo-elastic collisions occur among the components of the expanding fireball, that can affect the spectral shapes and the measurable yields of short-lived (strongly decaying) hadronic resonances. Once the particle density of the system is so low that the mean free path for elastic collisions is larger than the size of the system, the fireball freezes-out kinetically. At LHC energies, this is seen to occur when the system has reached temperatures of the order of $T_{kin} \approx 90$ MeV [5]. In such a dense and hot environment, composite objects with binding energies that are small with respect to the temperature of the system, appear as "fragile" objects. For instance, the binding energy of the deuteron is $B_{E,d} = 2.2$ MeV $\ll T_{chem}, T_{kin}$. As a matter of fact, the cross-section for pion-induced deuteron breakup is significantly larger than the typical (pseudo)-elastic cross-sections for the re-scattering of hadronic resonance decay products (check statement) [6, 7, 8]. Similarly, the elastic cross-section which drives the deuteron spectra to kinetic equilibration in central heavy-ion collisions [9] is smaller than the breakup cross-section [8]. Based on this, the deuterons produced at chemical freeze-out would be expected not to survive the hadronic phase of the medium expansion, yet their production is measured to be consistent to the predictions from statistical-thermal models and they develop also a non-zero elliptic flow which is consistent with a common radial expansion together with the non-composite hadrons [9]. Do similar estimates as Karel in Frascati. In addition, it was recently shown that the assumption of realistic eigenvolumina for light nuclei would lead to instabilities of the statistical/thermal model predictions [10]. Several solutions have been proposed to solve this "light (anti-)nuclei puzzle": (a.) a sudden freeze-out at the QGP-hadron phase boundary, (b.) the thermal production of these objects as compact quark bags [2], and (c.) the coincidence of coalescence mechanism with that of thermal production [11]. Data from rescattering of short-lived hadronic resonances indicate that the system undergoes a long-lasting hadronic phase before decoupling [12], thus strongly disfavouring hypothesis (a.). While hypothesis (b.) cannot presently be tested beyond the agreement of measured (anti-)nuclei production yields with statistical-thermal model predictions, hypothesis (c.) is scrutinised in the present work.

To this purpose, we compare to models the existing data from the Large Hadron Collider. For the first time, these data allow for the systematic study of the light (anti-)(hyper-)nuclei

Mass number	Nucleus	Compo-sition	B_E (MeV)	Spin J_A	(Charge) rms radius $\lambda_A{}^{meas}$ (fm)	Harmonic oscillator size parameter r_A (fm)	Refs.
A = 2	d	pn	2.224575 (9)	1	2.1413 ± 0.0025	3.2	[13, 14]
A = 3	^{3}H	pnn	8.4817986 (20)	1/2	1.755 ± 0.086	2.15	[15]
	^{3}He	ppn	7.7180428 (23)	1/2	1.959 ± 0.030	2.48	[15]
	$^3_\Lambda$H	pΛn	0.13 ± 0.05	1/2	$4.9 - 10.0$	$6.8 - 14.1$	[16, 17]
A = 4	^{4}He	ppnn	28.29566 (20)	0	1.6755 ± 0.0028	1.9	[18, 19]
	$^4_\Lambda$H	pΛnn	2.04 ± 0.04	0	$2.0 - 3.8$	$2.4 - 4.9$	[16, 17]
	$^4_{\Lambda\Lambda}$H	p$\Lambda\Lambda$n	$0.39 - 0.51$	1	$4.2 - 7.1$	$5.5 - 9.4$	[17]
	$^4_\Lambda$He	ppΛn	2.39 ± 0.03	0	$2.0 - 3.8$	$2.4 - 4.9$	[16, 17]

Table 1: Properties of nuclei and hyper-nuclei. B_E is the binding energy in MeV. The size of the nucleus is given in terms of the (charge) rms radius of the wavefunction, λ_A. The size parameter of the wave-function of the harmonic oscillator potential, r_A, is chosen such that the measured/expected rms is approximately reproduced. Details are given in Appendix A. Please note that proton rms charge radius λ_p is subtracted quadratically from the measured rms charge radius λ_A^{meas} of the nucleus $\lambda_A = \sqrt{(\lambda_A^{meas})^2 - \lambda_p^2}$ to account for the finite extension of the constituents. References are given in the last column. The spin of $^4_{\Lambda\Lambda}$H is discussed in the text of [17].

production as a function of the system and object size. In the nucleon-coalescence approach, nuclei are formed at kinetic freeze-out by coalescence of nucleons that are nearby in space and have similar velocities. The coalescence model is reviewed in Section 2, starting from its simplest form (uncorrelated nucleon emission from a point-like source) to the full space-time evolution picture as discussed in [11]. In section 3, a blast-wave parameterisation for particle transverse momentum spectra in combination with predictions from the statistical-thermal model for the yields is used as an alternative approach. The direct comparison of the two approaches and the comparison with data are discussed in section 4. We find that a systematic study of the coales-cence parameter B_A provides an important discrimination power between the two approaches. A comparison of the production rates of nuclei with similar mass but very different internal structure has already been suggested for the case of ^{4}He and ^{4}Li [20]. However, as the ^{4}Li is not stable with respect to strong decay, its measurement is experimentally very challenging and probably less constraining than the comparison with hyper-nuclei proposed here. In section ??, we propose that B_A is systematically measured in all collision systems by exploiting the large statistics sample that will be available with the LHC Run 3 and 4, in order to rule out or sup-port the aforementioned scenarios. As a matter of fact, the upcoming years of LHC data taking provide a unique opportunity to for the final understanding of (anti-)(hyper-)nuclei production. Setting a final word on the production mechanisms is not only in the interest of the heavy-ion community, but has a broader application in astrophysics and dark-matter searches, by repre-senting an essential input for the measurement of (anti-)nuclei in space with ongoing [21] and future [22, 23] experiments. In addition to this, the study of light(anti-)nuclei might serve as a baseline for understanding the debated nature of exotic states such as the X(3872), that has been interpreted as tetraquark state or hadronic molecule [24, 25].

2. Coalescence approach

2.1. Simple coalescence

In the coalescence picture, nucleons produced in the collision coalesce into nuclei if they are close in space and have similar velocities [26, 27]. For a nucleus with mass number $A = Z + N$, the coalescence probability is typically quantified in terms of the coalescence parameter B_A, which is defined as

$$E_A \frac{\mathrm{d}^3 N_A}{\mathrm{d}p_A^3} = B_A \left(E_\mathrm{p} \frac{\mathrm{d}^3 N_\mathrm{p}}{\mathrm{d}p_\mathrm{p}^3} \right)^Z \left(E_\mathrm{n} \frac{\mathrm{d}^3 N_\mathrm{n}}{\mathrm{d}p_\mathrm{n}^3} \right)^N \Bigg|_{\vec{p}_\mathrm{p} = \vec{p}_\mathrm{n} = \frac{\vec{p}_A}{A}} \ , \tag{1}$$

where $p_\mathrm{p,n}$ are the momenta of the proton and neutron and $E_{p,n}$ their energy. Since at LHC energies the number of produced protons and neutrons at midrapidity is expected to be equal, the equation simplifies to

$$E_A \frac{\mathrm{d}^3 N_A}{\mathrm{d}p_A^3} = B_A \left(E_\mathrm{p} \frac{\mathrm{d}^3 N_\mathrm{p}}{\mathrm{d}p_\mathrm{p}^3} \right)^A \Bigg|_{\vec{p}_\mathrm{p} = \frac{\vec{p}_A}{A}} \ . \tag{2}$$

Moreover, the LHC is particularly suited for the production of anti-nuclei, since the number of baryons and anti-baryons is essentially equal at midrapidity [28]. In a simple coalescence approach, the coalescence parameter is expected to be independent of p_T and of the object size with respect to the volume of particle emission (hereafter referred to as "source volume" or "source size"). In this naive expectation, the number of nuclei produced by coalescence increases with increasing number of nucleons produced in the collision. If the nucleon number increases with the event multiplicity, so does the number of (anti-)nuclei. While this picture is found to be approximately valid in pp and p–Pb collisions [29, 30], it breaks down in Pb–Pb collisions, that exhibit a strong decrease of B_A with the centrality of the collision [31]. In addition, the elliptic flow of deuterons cannot be explained by simple coalescence [32].

2.2. Full coalescence

In contrast to the simple approach described in the previous section, a more advanced coalescence model takes into account the size of the particle emission source, as the coalescence probability naturally decreases for two nucleons with similar momenta that are produced far apart in configuration space. While there are several approaches to address this effect [33, 34, 35], we rely in our study on the formalism proposed in [11].

In particular, the wave-function of the objects under study are approximated by the ground-state wave-functions of an isotropic spherical harmonic oscillator as in [11] with a characteristic size parameter r_A. For the deuteron $(A = 2)$ wave-function $\varphi_d(\vec{r})$, one obtains

$$\varphi_d(\vec{r}) = (\pi r_d^2)^{-3/4} \exp\left(-\frac{r^2}{2r_d^2} \right) \ . \tag{3}$$

For larger nuclei $(A > 2)$, analogous forms exist (see for instance [11] for the explicit form of A=3). The relation between the characteristic size parameter r_A and the rms of the wave-function was derived in [36] as

$$\lambda_A^2 = \frac{3}{2} \frac{A-1}{A} \frac{r_A^2}{2} \tag{4}$$

for point-like constituents. In particular, we obtain $r_d = \sqrt{8/3}\lambda_2$ for $A = 2$, $r_3 = \sqrt{2}\lambda_3$ for $A = 3$, and $r_4 = \sqrt{16/9}\lambda_4$ for $A = 4$ (see Appendix A for details).

This ansatz allows to derive in the following a set of analytic formulas which can be used for the calculation of coalescence predictions. In Tab. 1, we therefore do not list only the rms

of the wavefunction, but we also list the size parameter of the harmonic oscillator potential, r_A. The approximation of the wave-function with a gaussian form can be further refined with more realistic parameterisations, e.g. the Hulthen parameterisation for the deuteron or a Λ-deuteron parameterisation for the hyper-triton as done for central collisions in [37]. We encourage future more rigorous numerical studies which address the coalescence probabilities with more realistic wave-functions, but remain with the gaussian ansatz in the following in order to obtain more intuitive analytic solutions which highlight the sensitivity to the source (i.e. the centrality dependence) and the (hyper-)nucleus size. Consider mentioning the further approximations done by Uli in his paper, if there is time and how Uli's paper relates to the Wigner formalism.

In this approach, the quantum mechanical nature of the coalescence products is explicitly accounted for by means of an average quantum mechanical correction factor, $\langle C_A \rangle$. In the case of the deuteron, the quantum mechanical correction factor $\langle C_d \rangle$ has been approximated as

$$\langle C_d \rangle \approx \frac{1}{\left[1 + \left(\frac{r_d}{2R_\perp(m_T)}\right)^2\right]\sqrt{1 + \left(\frac{r_d}{2R_\parallel(m_T)}\right)^2}} \tag{5}$$

where r_d is the radius of the deuteron, $R_\perp$ and $R_\parallel$ are the lengths of homogeneity of the coalescence volume and m_T is the transverse mass of the coalescing nucleons. The size of the nucleus enters in the determination of the coalescence parameter B_2 via the quantum-mechanical correction factor $\langle C_d \rangle$, as well as the homogeneity volume $R_\perp^2 R_\parallel$, according to the relation

$$B_2 = \frac{3\pi^{3/2}\langle C_d \rangle}{2m_T R_\perp^2(m_T) R_\parallel(m_T)} \tag{6}$$

which is the main result of [11]. It is interesting to note that the coalescence parameter decreases with increasing volume, as expected. In addition to this, the quantum mechanical correction factor introduces a length scale defined by the deuteron size relative to the source size in the calculation of B_2, which reflects the coalescence probability. If we assume that $R_\perp \approx R_\parallel \approx R$, Eqs. 5 and 6 simplify to

$$\langle C_d \rangle \approx \left[1 + \left(\frac{r_d}{2R(m_T)}\right)^2\right]^{-3/2} \tag{7}$$

and

$$B_2 = \frac{3\pi^{3/2}\langle C_d \rangle}{2m_T R^3(m_T)}. \tag{8}$$

Figure 1 shows the source radius (R) dependence of the quantum-mechanical correction factor (on the left) and the coalescence parameter B_2 (on the right), calculated assuming (a.) a point-like nucleus $r_d = 0$, (b.) $r_d = 0.3$ fm similar to the value currently assumed in thermal model calculations [38], (c.) the actual value which reproduces the measured rms radius of the deuteron $r_d = 3.2$ fm [14], (d.) a larger, irrealistic value of $r_d = 10$ fm. As can be seen in Fig. 1, the quantum-mechanical correction factor leads to a significant suppression in the production of those objects whose radius is large compared to that of the source.

Following the approach and discussion presented in [39], Eq. 5 may be generalised as

$$\langle C_A \rangle = \prod_{i=1,2,3} \left(1 + \frac{r^2}{4R_i^2}\right)^{-\frac{1}{2}(A-1)} \tag{9}$$

for mass number A and the radii R_i which describe the volume of the emitting source. Similarly, the coalescence parameter B_A for a nucleus with mass number A and spin J_A is generalised in [11] as

$$B_A = \frac{2J_A + 1}{2^A} \frac{1}{\sqrt{A}} \langle C_A \rangle \left(\frac{(2\pi)^{3/2}}{m_T \prod_{i=1,2,3} R_i}\right)^{A-1}. \tag{10}$$
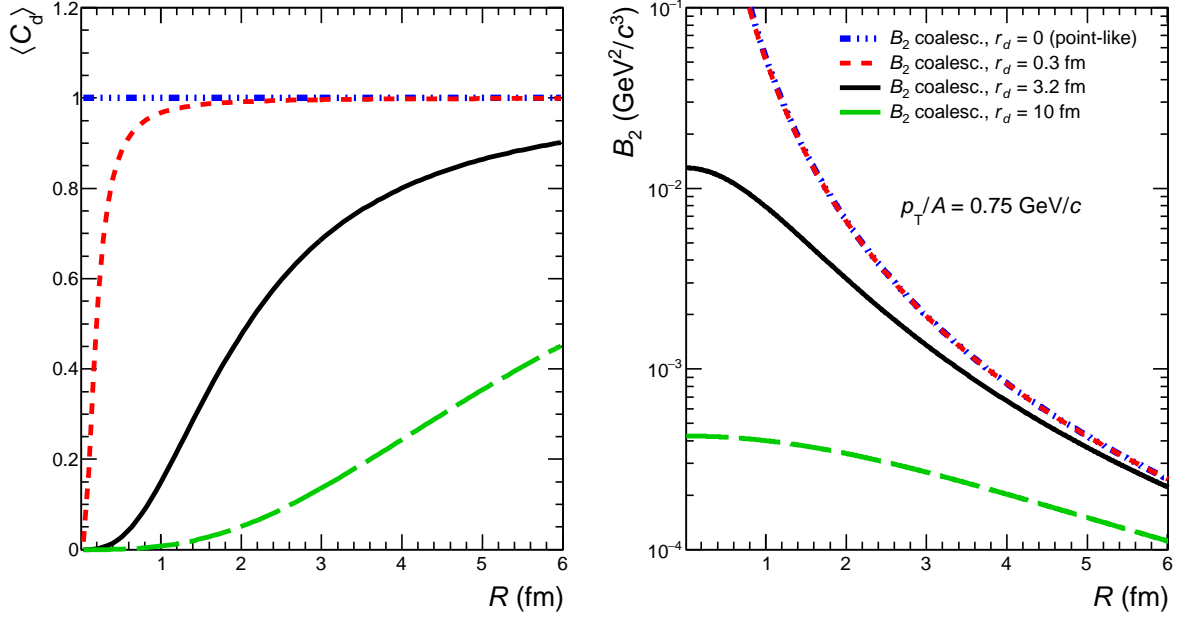
6

Figure 1: The quantum mechanical correction factor $\langle C_d \rangle$ (left panel, see Eq. 7) and the coalescence parameter B_2 for deuteron (right panel, see Eq. 8) as a function of the radius of the source, R, calculated assuming a size parameter for the deuteron $r_d = 0, 0.3, 3.2$ and 10 fm.

In particular, for the case of ^{3}He with $A = 3$ and $J = 1/2$, Eq. 10 becomes Eq. 9 presented in [39]:

$$B_3 = \frac{(2\pi)^3}{4\sqrt{3}} \langle C_3 \rangle (m_T \prod_{i=1,2,3} R_i)^{-2} \qquad (11)$$

where

$$\langle C_3 \rangle \approx \prod_{i=1,2,3} \left(1 + \frac{r_3^2}{4R_i^2} \right)^{-1}. \qquad (12)$$

In summary, one obtains under the assumption $R_1 \approx R_2 \approx R_3 \approx R$ (see details in next section) by combining Eq. 10 and Eq. 9 the following general expression for the coalescence parameter which can be compared to experimental data:

$$\boxed{B_A = \frac{J_A + 1}{2^A} \frac{1}{\sqrt{A}} \frac{1}{m_T^{A-1}} \left(\frac{2\pi}{R^2 + (\frac{r_A}{2})^2} \right)^{3/2(A-1)}} . \qquad (13)$$

2.3. Source volume

As in [11], we identify the source volume as the effective sub-volume of the whole system which is governed by the homogeneity length of the interacting nucleons. In addition, the same authors claim that this volume is experimentally accessible with Hanbury-Brown-Twiss (HBT) interferometry. The experimental results are typically obtained following the Bertsch-Pratt (BP) parameterisation ($R_{out}, R_{side}, R_{long}$), while the coalescence model described in Section 2 expresses the volume in terms of the Yano-Koonin-Podgoretskii (YKP) parameterisation. As discussed in Appendix C, we identify $R_\perp = R_{side}$ and $R_\parallel = R_{long}$, thus $R = (R_\perp^2 R_\parallel)^{1/3} \approx (R_{side}^2 R_{long})^{1/3}$.

Experimentally, the size of the effective volume can be controlled by selecting different collision geometries, i.e. different centrality classes [40]. In heavy-ion collisions the HBT radii are known

to scale with the cubic root of the average charged particle multiplicity density $\langle \mathrm{d}N_{\mathrm{ch}}/\mathrm{d}\eta \rangle^{1/3}$ [1], and to depend on the pair average transverse momentum $\langle k_{\mathrm{T}} \rangle$ [41]. In the following, we make the simplifying assumption that the scaling with $\langle \mathrm{d}N_{\mathrm{ch}}/\mathrm{d}\eta \rangle^{1/3}$ holds across collision systems, which is approximately fulfilled in data [42]. In contrast to [39], we therefore do not explicitly use the measured HBT radii in our study, but we derive the radii from the measured $\langle \mathrm{d}N_{\mathrm{ch}}/\mathrm{d}\eta \rangle$ according to the following relation:

$$R = a \langle \mathrm{d}N_{\mathrm{ch}}/\mathrm{d}\eta \rangle^{1/3} + b \tag{14}$$

The coefficients, $a = 0.339$ and $b = 0.128$ (in units of fm), have been determined by fitting linearly the ALICE data, and the parameterisation is reported in Fig. 2. These values are consistent with the radius from kaon femtoscopy for $m_{\mathrm{T}} \approx 1$ GeV/c in low-multiplicity pp collisions [43] and the radius from pion femtoscopy in high-multiplicity Pb–Pb collisions at the highest available $k_{\mathrm{T}} \approx 0.9$ GeV/c [1]. The highest k_{T} bin was chosen as it is closest in m_{T} to the lowest transverse momentum per nucleon ($p_{\mathrm{T}}/A \approx 0.8$ GeV/c) accessible by ALICE for the measurement of nuclei production. Ideally, one would use the proton femtoscopic radii for such study, but given that these measurements are not available in all collision systems, we assume that m_{T}-scaling holds for HBT radii [44].
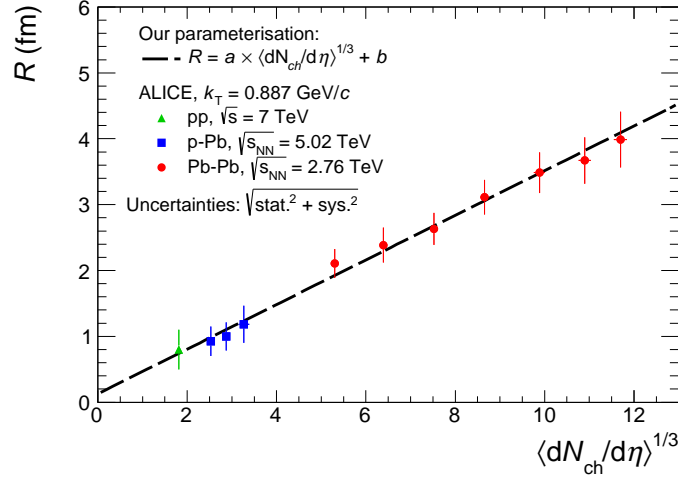

Figure 2: Parameterisation of the dependence of the source radius on multiplicity assumed in this paper, compared to HBT data from [1, 43].

- excess binding energy needs to be released to the system to make coalescence work

3. Statistical-thermal approach and blast-wave

In the statistical-thermal approach, the yields ($\mathrm{d}N/\mathrm{d}y$) of light anti- and hyper-nuclei are very sensitive to the chemical freeze-out temperature T_{chem} due to their large mass m and approximately scale as $\mathrm{d}N/\mathrm{d}y \propto \exp(-m/T_{chem})$. As a matter of fact, the chemical freeze-out temperature defines the only scale in this model, since at the LHC the chemical potentials which ensure the conservation of baryon number (μ_B), strangeness (μ_S), and electric charge (μ_Q) are negligible. In contrast to the coalescence approach, the current implementations [45, 46, 47] of the statistical-thermal model provide only p_{T}-integrated yields and not the full hadron spectra. In order to fill this gap, and for the purposes of this exercise, p_{T} spectra have been modelled using a blast-wave [48] parameterization. When extracting the predicted spectrum for a given particle species (proton, Λ, deuteron, ^{3}He), the parameters of the blast-wave (average radial

flow velocity $\langle \beta_T \rangle$, kinetic freeze-out temperature T_{kin}, and velocity profile n) are fixed to the values obtained from the simultaneous fit of the pion, kaon and proton spectra measured in each collision system and multiplicity event class by ALICE [5]. The normalisation is fixed using the p_T-integrated deuteron-to-pion ratio and ^{3}He-to-pion ratio predicted by the GSI-Heidelberg model with $T_{chem} = 156$ MeV, multiplied by the pion yield measured by ALICE [5]. This choice is motivated by the fact that the measured proton yield is seen to be slightly underestimated by the thermal model predictions at the LHC [49]. In the case of hyper-triton, a slightly different procedure is chosen, namely the normalisation for $^3_\Lambda$H is extracted from the statistical-thermal model prediction of the strangeness population factor S_3 multiplied by the measured Λ/p ratio [50, 5] and the measured ^{3}He yield [31]. Based on the thus obtained spectra, we calculate the corresponding coalescence parameters for a given p_T/A and compare it with coalescence expectations. Because we use experimental data to constrain the blast-wave prediction as well as the normalisation, and because such data are provided for given centrality/multiplicity classes, we use the corresponding $\langle \mathrm{d}N_{ch}/\mathrm{d}\eta \rangle$ in the same class to estimate the system radius based on the parameterisation discussed in Sec. 2.3. In contrast to the coalescence approach which explicitly depends on the size of the produced object with respect to the system size, the object size does not enter in the formulation of the blast-wave model, which as a simplified hydrodynamic model treats the system based as a continuum and is not particle based. The thermal model on the other hand, implements eigenvolume corrections where the object radius is fixed as an external parameter ($r = 0.3$ fm in the case of baryons for the GSI-Heidelberg prediction used here). We refer to the literature for the extensive discussions on the validity of the eigenvolume correction for light anti- and hyper-nuclei [10] and the relation with the possible production of these objects as compact quark bags [2].

4. Comparison with experimental data

4.1. Constraining the source volume with data

Data on anti- and hyper-nuclei production at LHC energies and different collision systems have been released by the ALICE Collaboration in recent years [31, 29, 32, 51]. In Fig. 3 we compare the coalescence parameter B_2 from the coalescence model (see Eqs. 6 and 8, with $r_d = 3.2$ fm) with the ALICE data. First, the parameterisation of the system radius fitted to the HBT data as described in Sec. 2.3 is used to map the $\langle \mathrm{d}N_{ch}/\mathrm{d}\eta \rangle$ to the source size (datapoints shown in the two left panels). We notice already at this point that the coalescence volume from our extracted parameterisation of the HBT radii leads to discrepancies with respect to the curve from the coalescence calculation, and in particular, we notice that the model would require a larger radius for a given value of B_2.

Therefore, in a second step the radius is tuned such that the data points for (anti-) deuterons fall onto the coalescence prediction (solid markers). We find that the parameters of Eq. 14 turn out to be $a \approx 0.473$ and $b \approx 0$. With this second parameterisation, we investigate also the agreement of the model with the measured coalescence parameter B_3. As shown in Fig. 3, also in the case of B_3, a tension between the model and the data is found which ameliorates with the parameterisation which is tuned to the (anti-)deuteron data. The strength of this approach is given by the fact that the coalescence volume is constrained with the more differential (anti-)deuteron data assuming that it is the same for all fragile anti- and hyper-nuclei. It is also noteworthy that any change of the radii parameterisation would result in a shift along the x axis of both B_2 and B_3 data points in the same way, while the theoretical coalescence curve would not be affected.
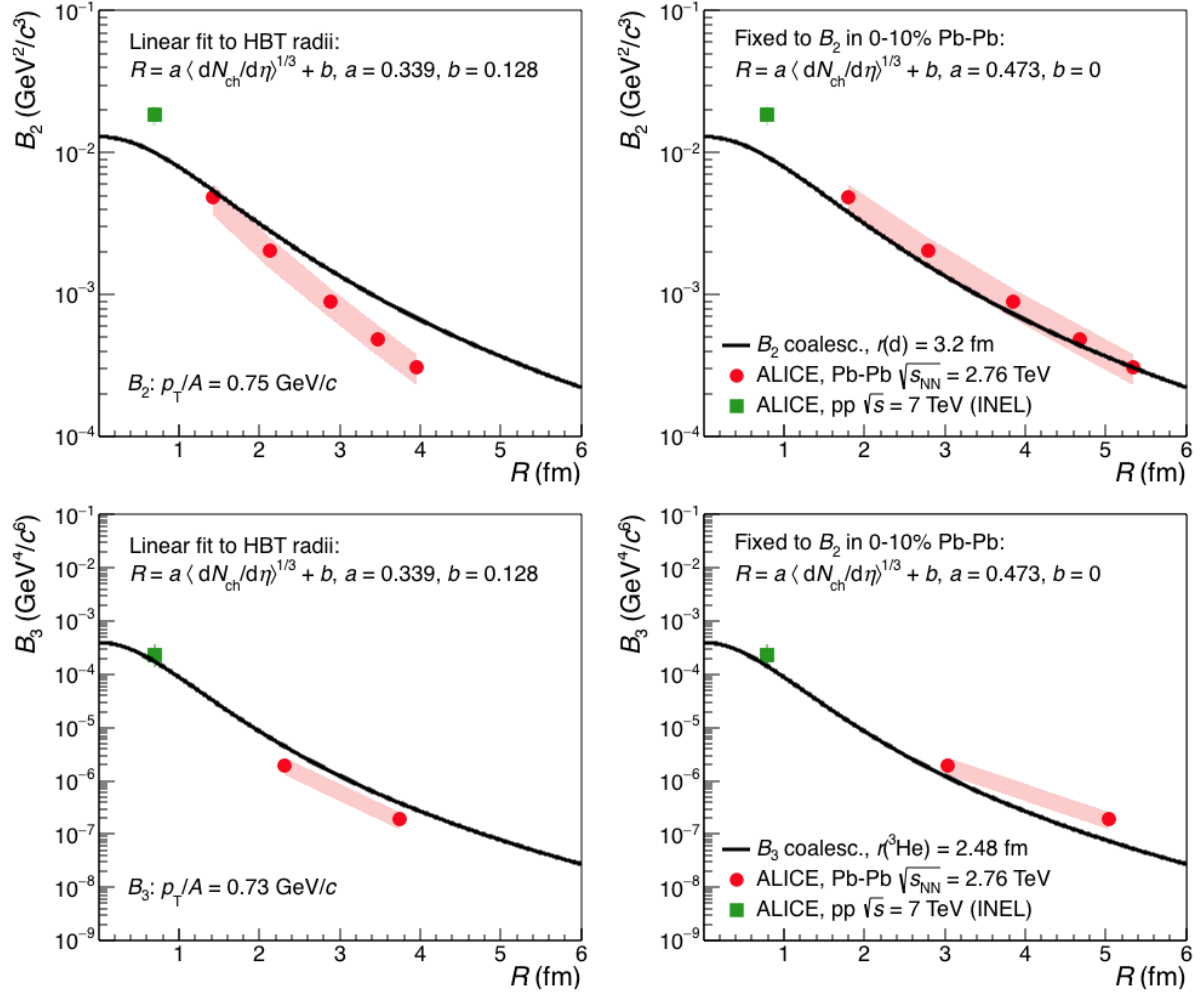
Figure 3: Comparison of the ALICE data from [31, 29] with the coalescence prediction for two different mappings of the $\langle dN_{ch}/d\eta \rangle$ to the system size R: (left panels) the parameterisation fitted to the HBT radii, (right panels) the parameterisation tuned to the B_2 values in central Pb-Pb collisions.

4.2. Thermal and coalescence model for A=2,3 anti- and hyper-nuclei

- add a three-panel plot for deuteron, he and hyper-triton with different radii for hyper-triton from 10fm to 3fm and for the excited state of the hyper-triton!!
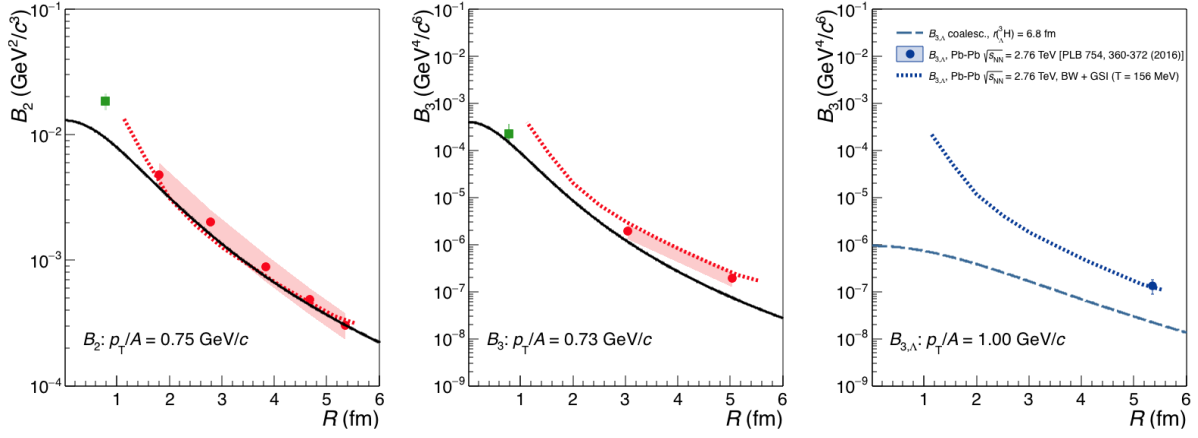

Figure 4: Comparison of the ALICE data from [31, 29] with the thermal model expectations and the coalescence prediction which is tuned to B_2 values in central Pb-Pb collisions.

5. Summary, conclusions, and outlook

We conclude that (c.) appears unlikely, thus leaving (b.) as a viable option, at least with our present knowledge of the hypertriton size.

In the following, we summarise our main conclusions:

1. Thermal and coalescence models give similar predictions for the production of A=2 and A=3 (anti-)nuclei in heavy-ion collisions for a source volume that is constrained by experimental data on (anti-)deuteron production.

2. Thermal and coalescence models give very different predictions for the production of hyper-tritons as a function of source volume in pp, p-Pb, and Pb-Pb collisions. In particular, the yield of hyper-tritons appears to be suppressed by a factor of about ???? in pp collisions with respect ot the production of ^{3}He.

In a follow-up publication, we will extend the study presented here to predictions for the A=4 systems introduced in Tab. **??** and to more exotic QCD objects like the X(3827). These predictions will be of outmost importance for the currently prepared physics case for LHC Run 3 & 4 and beyond.

A. Relation to the Sato-Yazaki coalescence model

The approach of Sato and Yazaki [33] is based on a density matrix model and includes explicitly the system size dependence and wave-function dependence of the coalescence process albeit it assumes a sudden approximation when particles cease their interactions (sudden freeze-out) and thus neglects the collective expansion of the medium as in [11]. Moreover, it assumes no correlation between different nucleons and no correlation between coordinates in space and momentum (in a heavy ion collisions, such correlations are consequence of hydrodynamical flow). In [33], the coalescence process to form a nucleus with mass number $A = Z + N$ is formulated in terms of the momentum per nucleon (p) as

$$\frac{\gamma_A}{\sigma_{A,0}} \frac{d^3\sigma_A}{d^3p} = \left(\frac{4}{3}\pi p_0^3\right)^{A-1} \frac{1}{Z!N!} \left(\frac{\gamma_p}{\sigma_{p,0}} \frac{d^3\sigma_p}{d^3p_p}\right)^Z \left(\frac{\gamma_n}{\sigma_{n,0}} \frac{d^3\sigma_n}{d^3p_n}\right)^N \tag{15}$$

where γ_A and $\gamma_{p,n}$ are the Lorentz factors for the nucleus and the nucleons, respectively. Assuming that the proton and neutron emission probabilities are equal and that $p_p \approx p_n \equiv p$, this expression relates to the B_A as defined by our Lorentz invariant Eq.(2) as

$$B_A = \left(\frac{4}{3}\pi p_0^3\right)^{A-1} \frac{M}{m^A} \frac{1}{A^3} \frac{1}{Z!N!} \tag{16}$$

where the factor $\frac{1}{A^3}$ results from the transformation of $p_A \to A p_{p,n}$ and M corresponds to the nucleus mass and m to the nucleon mass. This expression can be further simplified via the approximation $M \approx Am$ to

$$B_A = \left(\frac{4}{3}\pi p_0^3\right)^{A-1} \frac{1}{m^{A-1}} \frac{1}{A^2} \frac{1}{Z!N!} . \tag{17}$$

For nuclei up to $A = 4$ and the non-relativistic case, Sato and Yazaki derive the following relations for the coalescence momentum p_0,

$$A = 2 \qquad\qquad \frac{4}{3}\pi p_0^3 = \frac{3}{4} 2^{3/2} (4\pi)^{3/2} \left(\frac{\nu_2 \nu}{\nu_2 + \nu}\right)^{3/2} \tag{18}$$

$$A = 3 \qquad\qquad \frac{1}{2}\left(\frac{4}{3}\pi p_0^3\right)^2 = \frac{1}{4} 3^{3/2} (4\pi)^3 \left(\frac{\nu_3 \nu}{\nu_3 + \nu}\right)^3 \tag{19}$$

$$A = 4 \qquad\qquad \frac{1}{4}\left(\frac{4}{3}\pi p_0^3\right)^3 = \frac{1}{16} 4^{3/2} (4\pi)^{9/2} \left(\frac{\nu_4 \nu}{\nu_4 + \nu}\right)^{9/2} \tag{20}$$

where the size parameter ν relates to the rms radius R_{rms} of the emission source as $\nu = \sqrt{\frac{3}{2R_{rms}}}$, and ν_A is the size parameter of the nucleus.

Following the generalisation in [34], we thus propose the following parameterisation for the coalescence parameter

$$B_A = \frac{2J_A + 1}{2^A} A^{3/2} (4\pi)^{\frac{3}{2}(A-1)} \left(\frac{\nu_A \nu}{\nu_A + \nu}\right)^{\frac{3}{2}(A-1)} \frac{1}{m^{A-1}} \frac{1}{A^2} \tag{21}$$

$$= \frac{2J_A + 1}{2^A} \frac{1}{m^{A-1}} \frac{1}{\sqrt{A}} (4\pi)^{\frac{3}{2}(A-1)} \left(\frac{\nu_A \nu}{\nu_A + \nu}\right)^{\frac{3}{2}(A-1)} , \tag{22}$$

indicating with J_A the spin of the nucleus. Once again, the ν_A parameter corresponds to the size parameter of the nucleus wave-function, which is assumed to be gaussian (solution to the spherical harmonic oscillator potential) of the form [33, 35]:

$$\phi_A = C \exp\left(-\frac{1}{2}\nu_A \sum_{i=1}^{A}(\vec{x}_i - \vec{X})^2\right) \tag{23}$$

with an appropriate normalisation factor C and the coordinate vector $\vec{X}$ of the centre-of-mass system.

We have also verified that our generalisation of Sato-Yazaki provided by Eq. 22 and the expression derived from Heinz in Eq. 9 become consistent in the limit $R_{rms} \approx R \to 0$ (point-like source) and $p_T \to 0$ (static source), provided that one identifies $\nu_A = 2/r_A^2$. Incidentally, the same relation between ν_A and r_A can be derived by a straightforward comparison of the nucleus wave-functions employed by the same authors [11, 33].

The parameter ν_A is typically chosen such that the measured rms charge radius λ_A is reproduced. The relation between λ_A and ν_A is obtained by a transformation to the Jacobi variables and performing the integration (see Appendix B). In particular, one obtains for $A < 5$:

$$A = 2 \qquad \nu_2 = \frac{3}{4\lambda_2^2} \tag{24}$$

$$A = 3 \qquad \nu_3 = \frac{1}{\lambda_3^2} \tag{25}$$

$$A = 4 \qquad \nu_4 = \frac{9}{8\lambda_4^2} \tag{26}$$

B. RMS of a gaussian wave-function for A=4

In this appendix, we show the calculation of the RMS of a gaussian wave-function with the example of A=4. We start from the wave-function

$$\phi_{A=4} = C_4 \exp\left(-\frac{1}{2}\nu_4 \sum_{i=1}^{4}(\vec{x}_i - \vec{X})^2\right). \tag{27}$$

Then we introduce the Jacobi variables which are given by

$$\vec{X} = \frac{1}{4}(\vec{x_1} + \vec{x_2} + \vec{x_3} + \vec{x_4}) \tag{28}$$

$$\vec{r_1} = \vec{x_2} - \vec{x_1} \tag{29}$$

$$\vec{r_2} = \vec{x_3} - \frac{1}{2}(\vec{x_1} + \vec{x_2}) \tag{30}$$

$$\vec{r_3} = \vec{x_4} - \frac{1}{3}(\vec{x_1} + \vec{x_2} + \vec{x_3}). \tag{31}$$

In this parameterisation we can express the squared distance of each nucleon with respect to the centre-of-mass as

$$\sum_{i=1}^{4}(\vec{x}_i - \vec{X})^2 = \frac{1}{4}\left(2\vec{r_1} + \frac{8}{3}\vec{r_2} + 3\vec{r_3}\right). \tag{32}$$

For the following integral calculations we determine the Jacobian as

$$\mathrm{d}R\mathrm{d}r_1\mathrm{d}r_2\mathrm{d}r_3 = |\det\frac{\partial(R, r_1, r_2, r_3)}{\partial(x_1, x_2, x_3, x_4)}| \, \mathrm{d}x_1\mathrm{d}x_2\mathrm{d}x_3\mathrm{d}x_4 \tag{33}$$

$$= \begin{vmatrix} \frac{\partial R}{\partial x_1} & \frac{\partial r_1}{\partial x_1} & \frac{\partial r_2}{\partial x_1} & \frac{\partial r_3}{\partial x_1} \\ \frac{\partial R}{\partial x_2} & \frac{\partial r_1}{\partial x_2} & \frac{\partial r_2}{\partial x_2} & \frac{\partial r_3}{\partial x_2} \\ \frac{\partial R}{\partial x_3} & \frac{\partial r_1}{\partial x_3} & \frac{\partial r_2}{\partial x_3} & \frac{\partial r_3}{\partial x_3} \\ \frac{\partial R}{\partial x_4} & \frac{\partial r_1}{\partial x_4} & \frac{\partial r_2}{\partial x_4} & \frac{\partial r_3}{\partial x_4} \end{vmatrix} \mathrm{d}x_1\mathrm{d}x_2\mathrm{d}x_3\mathrm{d}x_4 \tag{34}$$

$$= \begin{vmatrix} \frac{1}{4} & -1 & -\frac{1}{2} & -\frac{1}{3} \\ \frac{1}{4} & 1 & -\frac{1}{2} & -\frac{1}{3} \\ \frac{1}{4} & 0 & 1 & -\frac{1}{3} \\ \frac{1}{4} & 0 & 0 & 1 \end{vmatrix} \mathrm{d}x_1\mathrm{d}x_2\mathrm{d}x_3\mathrm{d}x_4 \tag{35}$$

$$= 1 \cdot \mathrm{d}x_1\mathrm{d}x_2\mathrm{d}x_3\mathrm{d}x_4. \tag{36}$$

From the requirement $\int |\phi|^2 \mathrm{d}\vec{r_1}\mathrm{d}\vec{r_2}\mathrm{d}\vec{r_3} = 1$, we thus obtain for the normalisation constant C_4:

$$\frac{1}{C_4^2} = \int \exp^2\left(-\frac{1}{2}\nu_4\left(\frac{1}{2}r_1^2 + \frac{2}{3}r_2^2 + \frac{3}{4}r_3^2\right)\right)\mathrm{d}\vec{r_1}\mathrm{d}\vec{r_2}\mathrm{d}\vec{r_3} \tag{37}$$

where the integration in spherical coordinates is performed with $\mathrm{d}\vec{r_1} = 4\pi r_1^2\mathrm{d}r_1, \mathrm{d}\vec{r_2} = \ldots$ which gives

$$\frac{1}{C_4^2} = (4\pi)^3 \underbrace{\int_0^\infty r_1^2 \exp\left(-\frac{1}{2}\nu_4 r_1^2\right)\mathrm{d}r_1}_{\frac{\sqrt{\pi}}{4}\frac{1}{(\frac{1}{2}\nu_4)^{3/2}}} \underbrace{\int_0^\infty r_2^2 \exp\left(-\frac{2}{3}\nu_4 r_2^2\right)\mathrm{d}r_2}_{\frac{\sqrt{\pi}}{4}\frac{1}{(\frac{2}{3}\nu_4)^{3/2}}} \underbrace{\int_0^\infty r_3^2 \exp\left(-\frac{3}{4}\nu_4 r_3^2\right)\mathrm{d}r_3}_{\frac{\sqrt{\pi}}{4}\frac{1}{(\frac{3}{4}\nu_4)^{3/2}}} \quad (38)$$

$$= \left(\frac{\pi}{\nu_A}\right)^{9/2} 4^{3/2} \tag{39}$$

$$\Rightarrow C_4 = \left(\frac{\nu_A^3}{4\pi^3}\right)^{3/4} . \tag{40}$$

325 For the rms, we obtain accordingly:

$$\lambda_4^2 = \frac{1}{4}\langle\phi|\sum_{i=1}^4 (\vec{x}_i - \vec{X})^2|\phi\rangle \tag{41}$$

$$= \int \frac{1}{4}\sum_{i=1}^4 (\vec{x}_i - \vec{X})^2 |\phi|^2 \mathrm{d}\vec{x}_1 \mathrm{d}\vec{x}_2 \mathrm{d}\vec{x}_3 \mathrm{d}\vec{x}_4 \tag{42}$$

$$= \frac{C_4^2}{4}\int \left(\frac{1}{2}r_1^2 + \frac{2}{3}r_2^2 + \frac{3}{4}r_3^2\right) \exp^2\left(-\frac{1}{2}\nu_4\left(\frac{1}{2}r_1^2 + \frac{2}{3}r_2^2 + \frac{3}{4}r_3^2\right)\right)\mathrm{d}\vec{r}_1 \mathrm{d}\vec{r}_2 \mathrm{d}\vec{r}_3 \tag{43}$$

$$= \frac{C_4^2}{4}\Big(\frac{1}{2}\underbrace{\int r_1^2 \exp\left(-\frac{1}{2}\nu_A r_1^2\right)\exp\left(-\frac{2}{3}\nu_A r_2^2\right)\exp\left(-\frac{3}{4}\nu_A r_3^2\right)\mathrm{d}\vec{r}_1 \mathrm{d}\vec{r}_2 \mathrm{d}\vec{r}_3}_{\text{I}} \tag{44}$$

$$+ \frac{2}{3}\underbrace{\int r_2^2 \exp\left(-\frac{1}{2}\nu_A r_1^2\right)\exp\left(-\frac{2}{3}\nu_A r_2^2\right)\exp\left(-\frac{3}{4}\nu_A r_3^2\right)\mathrm{d}\vec{r}_1 \mathrm{d}\vec{r}_2 \mathrm{d}\vec{r}_3}_{\text{II}} \tag{45}$$

$$+ \frac{3}{4}\underbrace{\int r_3^2 \exp\left(-\frac{1}{2}\nu_A r_1^2\right)\exp\left(-\frac{2}{3}\nu_A r_2^2\right)\exp\left(-\frac{3}{4}\nu_A r_3^2\right)\mathrm{d}\vec{r}_1 \mathrm{d}\vec{r}_2 \mathrm{d}\vec{r}_3}_{\text{III}}\Big) \tag{46}$$

326 The first summand I can be calculated with $\mathrm{d}\vec{r}_1 \mathrm{d}\vec{r}_2 \mathrm{d}\vec{r}_3 = (4\pi)^3 r_1^2 r_2^2 r_3^2 \mathrm{d}r_1 \mathrm{d}r_2 \mathrm{d}r_3$ as

$$\text{I} = \frac{1}{2}(4\pi)^3 \cdot \int_0^\infty r_1^2 \exp\left(-\frac{1}{2}\nu_A r_1^2\right)\mathrm{d}r_1 \cdot \int_0^\infty \exp\left(-\frac{2}{3}\nu_A r_2^2\right)\mathrm{d}r_2 \cdot \int_0^\infty \exp\left(-\frac{3}{4}\nu_A r_3^2\right)\mathrm{d}r_3 \tag{47}$$

$$= \frac{1}{2}(4\pi)^3 \cdot \frac{3\sqrt{\pi}}{8}\frac{1}{(\frac{1}{2}\nu_A)^{5/2}} \cdot \frac{\sqrt{\pi}}{4}\frac{1}{(\frac{2}{3}\nu_A)^{3/2}} \cdot \frac{\sqrt{\pi}}{4}\frac{1}{(\frac{3}{4}\nu_A)^{3/2}} . \tag{48}$$

327 The other two summands II and III are evaluated accordingly and we thus obtain for the rms:

$$\lambda_4^2 = \frac{C_4^2}{4}(\text{I} + \text{II} + \text{III}) \tag{49}$$

$$= \frac{C_4^2}{4}(4\pi)^3 \frac{3\pi^{3/2}}{8 \cdot 4^2 \cdot \nu_A^{11/2}} \underbrace{\left(\frac{\frac{1}{2}}{(\frac{1}{2})^{5/2}(\frac{2}{3})^{3/2}(\frac{3}{4})^{3/2}} + \frac{\frac{2}{3}}{(\frac{1}{2})^{3/2}(\frac{2}{3})^{5/2}(\frac{3}{4})^{3/2}} + \frac{\frac{3}{4}}{(\frac{1}{2})^{3/2}(\frac{2}{3})^{3/2}(\frac{3}{4})^{5/2}}\right)}_{=24}$$

$$\tag{50}$$

$$= \frac{9}{8\nu_A} . \tag{51}$$

15

C. HBT radii in Bertsch-Pratt and Yano-Koonin-Podgoretskii parameterisation for comparison with coalescence models

The results of HBT analyses are typically presented in either the Bertsch-Pratt (R_{out}, R_{side}, R_{long}) or the Yano-Koonin-Podgoretskii ($R_{\perp}$, R_0, $R_{\parallel}$) parameterization. The ALICE HBT results [41, 1] are given in the Bertsch-Pratt convention, whereas the coalescence parameter is derived in [11] by expressing the dependence on the volume in terms of the Yano-Koonin-Podgoretskii (YKP) parameterisation. The transformation between the two parameterisations is best presented in [52] in the equations (W 3.48) to (W 3.52)[1]:

$$
\begin{align}
R_{side}^2 &= R_{\perp}^2 \,, \tag{52}\\
R_{diff}^2 &= R_{out}^2 - R_{side}^2 = \beta_{\perp}^2 \gamma^2 (R_0^2 + v^2 R_{\parallel}^2) \,, \tag{53}\\
R_{long}^2 &= (1 - \beta_l^2) R_{\parallel}^2 + \gamma^2 (\beta_l - v)^2 (R_0^2 + v^2 R_{\parallel}^2) \,, \tag{54}\\
R_{ol}^2 &= \beta_{\perp} (-\beta_l R_{\parallel}^2 + \gamma^2 (\beta_l - v)(R_0^2 + v^2 R_{\parallel}^2)) \,. \tag{55}
\end{align}
$$

We immediately identify that $R_{\perp}^2$ can be identified with R_{side}^2. Following the reasoning and the nomenclature in [52] (W 3.52-3.53), the above equations can be inverted and $R_{\parallel}^2$ can be expressed as

$$
\begin{align}
R_{\parallel}^2 &= B - v \cdot C \,, \tag{56}\\
&= R_{long}^2 - 2\frac{\beta_l}{\beta_{\perp}} R_{ol}^2 + \frac{\beta_l^2}{\beta_{\perp}^2} R_{diff}^2 - v \cdot \left(-\frac{1}{\beta_{\perp}} R_{ol}^2 + \frac{\beta_l}{\beta_{\perp}^2} R_{diff}^2 \right) \,. \tag{57}
\end{align}
$$

As it turns out all corrections which are subtracted from R_{long}^2 can be neglected. First, we notice that the cross term R_{ol} vanishes if the measured fireball is longitudinally boost-invariant, which is a valid approximation for the rapidity ranges studied here. The remaining terms are all proportional to β_l, which is also $\beta_l = 0$ by definition of the rest frame for a longitudinally-boosted invariant system. In summary, we can consider $R_{\perp} = R_{side}$ and $R_{\parallel} = R_{long}$ for the present study.

Acknowledgements

References

[1] **ALICE** Collaboration, J. Adam *et al.*, "Centrality dependence of pion freeze-out radii in Pb-Pb collisions at $\sqrt{s}_{NN} = 2.76$ TeV," *Phys. Rev.* **C93** no. 2, (2016) 024905, arXiv:1507.06842 [nucl-ex].

[2] A. Andronic, P. Braun-Munzinger, K. Redlich, and J. Stachel, "Decoding the phase structure of QCD via particle production at high energy," arXiv:1710.09425 [nucl-th].

[3] A. Andronic, P. Braun-Munzinger, J. Stachel, and H. Stocker, "Production of light nuclei, hypernuclei and their antiparticles in relativistic nuclear collisions," *Physics Letters B* **697** no. 3, (2011) 203 – 207. http://www.sciencedirect.com/science/article/pii/S0370269311001006.

---

[1]The equations in [52] are denoted as (W...) in order to distinguish them from the equations presented in this paper.

[4] **HotQCD** Collaboration, A. Bazavov *et al.*, "Equation of state in (2+1)-flavor QCD," *Phys. Rev.* **D90** (2014) 094503, arXiv:1407.6387 [hep-lat].

[5] **ALICE** Collaboration, B. Abelev *et al.*, "Centrality dependence of π, K, p production in Pb-Pb collisions at $\sqrt{s_{NN}} = 2.76$ TeV," *Phys. Rev.* **C88** (2013) 044910, arXiv:1303.0737 [hep-ex].

[6] H. Garcilazo, "PION DEUTERON BREAKUP IN THE REGION OF THE (3,3) RESONANCE," *Phys. Rev. Lett.* **48** (1982) 577–580.

[7] S. A. Bass *et al.*, "Microscopic models for ultrarelativistic heavy ion collisions," *Prog. Part. Nucl. Phys.* **41** (1998) 255–369, arXiv:nucl-th/9803035 [nucl-th]. [Prog. Part. Nucl. Phys.41,225(1998)].

[8] J. Schukraft, "QM2017: Status and Key open Questions in Ultra-Relativistic Heavy-Ion Physics," *Nucl. Phys.* **A967** (2017) 1–10, arXiv:1705.02646 [hep-ex].

[9] **ALICE** Collaboration, S. Acharya *et al.*, "Measurement of deuteron spectra and elliptic flow in Pb-Pb collisions at $\sqrt{s_{\mathrm{NN}}} = 2.76$ TeV at the LHC," *Eur. Phys. J.* **C77** no. 10, (2017) 658, arXiv:1707.07304 [nucl-ex].

[10] V. Vovchenko and H. Stoecker, "Analysis of hadron yield data within hadron resonance gas model with multi-component eigenvolume corrections," *J. Phys. Conf. Ser.* **779** no. 1, (2017) 012078, arXiv:1610.02346 [nucl-th].

[11] R. Scheibl and U. W. Heinz, "Coalescence and flow in ultrarelativistic heavy ion collisions," *Phys. Rev.* **C59** (1999) 1585–1602, arXiv:nucl-th/9809092 [nucl-th].

[12] **ALICE** Collaboration, B. B. Abelev *et al.*, "$K^*(892)^0$ and ?(1020) production in Pb-Pb collisions at $\sqrt{sNN} = 2.76$ TeV," *Phys. Rev.* **C91** (2015) 024609, arXiv:1404.0495 [nucl-ex].

[13] C. Van Der Leun and C. Alderliesten, "The deuteron binding energy," *Nucl. Phys.* **A380** (1982) 261–269.

[14] P. J. Mohr, D. B. Newell, and B. N. Taylor, "CODATA Recommended Values of the Fundamental Physical Constants: 2014," *Rev. Mod. Phys.* **88** no. 3, (2016) 035009, arXiv:1507.07956 [physics.atom-ph].

[15] J. E. Purcell and C. G. Sheu, "Nuclear Data Sheets for A = 3," *Nucl. Data Sheets* **130** (2015) 1–20.

[16] D. H. Davis, "50 years of hypernuclear physics. I. The early experiments," *Nucl. Phys.* **A754** (2005) 3–13.

[17] H. Nemura, Y. Suzuki, Y. Fujiwara, and C. Nakamoto, "Study of light Lambda and Lambda-Lambda hypernuclei with the stochastic variational method and effective Lambda N potentials," *Prog. Theor. Phys.* **103** (2000) 929–958, arXiv:nucl-th/9912065 [nucl-th].

[18] M. Wang, G. Audi, F. Kondev, W. Huang, S. Naimi, and X. Xu, "The ame2016 atomic mass evaluation (ii). tables, graphs and references," *Chinese Physics C* **41** no. 3, (2017) 030003. http://stacks.iop.org/1674-1137/41/i=3/a=030003.

[19] I. Angeli and K. P. Marinova, "Table of experimental nuclear ground state charge radii: An update," *Atom. Data Nucl. Data Tabl.* **99** no. 1, (2013) 69–95.

[20] S. Bazak and S. Mrowczynski, "^{4}He vs. ^{4}Li and production of light nuclei in relativistic heavy-ion collisions," arXiv:1802.08212 [nucl-th].

[21] **AMS** Collaboration, J. Alcaraz *et al.*, "Search for anti-helium in cosmic rays," *Phys. Lett.* **B461** (1999) 387–396, arXiv:hep-ex/0002048 [hep-ex].

[22] S. Schael, "AMS-100 - A Magnetic Spectrometer at Lagrange Point 2, presentation at AMS days La Palma 2018.".

[23] **GAPS** Collaboration, T. Aramaki, C. J. Hailey, S. E. Boggs, P. von Doetinchem, H. Fuke, S. I. Mognet, R. A. Ong, K. Perez, and J. Zweerink, "Antideuteron Sensitivity for the GAPS Experiment," *Astropart. Phys.* **74** (2016) 6–13, arXiv:1506.02513 [astro-ph.HE].

[24] A. Esposito, A. L. Guerrieri, L. Maiani, F. Piccinini, A. Pilloni, A. D. Polosa, and V. Riquer, "Observation of light nuclei at ALICE and the X(3872) conundrum," *Phys. Rev.* **D92** no. 3, (2015) 034028, arXiv:1508.00295 [hep-ph].

[25] **ExHIC** Collaboration, S. Cho *et al.*, "Exotic Hadrons from Heavy Ion Collisions," *Prog. Part. Nucl. Phys.* **95** (2017) 279–322, arXiv:1702.00486 [nucl-th].

[26] S. T. Butler and C. A. Pearson, "Deuterons from High-Energy Proton Bombardment of Matter," *Phys. Rev.* **129** (1963) 836–842.

[27] J. I. Kapusta, "Mechanisms for deuteron production in relativistic nuclear collisions," *Phys. Rev.* **C21** (1980) 1301–1310.

[28] **ALICE** Collaboration, E. Abbas *et al.*, "Mid-rapidity anti-baryon to baryon ratios in pp collisions at $\sqrt{s}$ = 0.9, 2.76 and 7 TeV measured by ALICE," *Eur. Phys. J.* **C73** (2013) 2496, arXiv:1305.1562 [nucl-ex].

[29] **ALICE** Collaboration, S. Acharya *et al.*, "Production of deuterons, tritons, ^{3}He nuclei and their antinuclei in pp collisions at $\sqrt{s}$ = 0.9, 2.76 and 7 TeV," *Phys. Rev.* **C97** no. 2, (2018) 024615, arXiv:1709.08522 [nucl-ex].

[30] **ALICE** Collaboration, S. Acharya *et al.*, "Multiplicity dependence of (anti-)nuclei production in p-Pb collisions at $\sqrt{s_{\mathrm{NN}}}$ = 5.02 TeV," *To be published* **xx** (2018) yy, arXiv:xxxx.xxxx [nucl-ex].

[31] **ALICE** Collaboration, J. Adam *et al.*, "Production of light nuclei and anti-nuclei in pp and Pb-Pb collisions at energies available at the CERN Large Hadron Collider," *Phys. Rev.* **C93** no. 2, (2016) 024917, arXiv:1506.08951 [nucl-ex].

[32] **ALICE** Collaboration, S. Acharya *et al.*, "Measurement of deuteron spectra and elliptic flow in Pb-Pb collisions at $\sqrt{s_{\mathrm{NN}}}$ = 2.76 TeV at the LHC," *Eur. Phys. J.* **C77** no. 10, (2017) 658, arXiv:1707.07304 [nucl-ex].

[33] H. Sato and K. Yazaki, "On the coalescence model for high-energy nuclear reactions," *Phys. Lett.* **98B** (1981) 153–157.

[34] J. L. Nagle, B. S. Kumar, D. Kusnezov, H. Sorge, and R. Mattiello, "Coalescence of deuterons in relativistic heavy ion collisions," *Phys. Rev.* **C53** (1996) 367–376.

[35] J. C. Bergstrom, "6 Li electromagnetic form factors and phenomenological cluster models," *Nucl. Phys.* **A327** (1979) 458–476.

[36] A. Shebeko, P. Papakonstantinou, and E. Mavrommatis, "The One-body and two-body density matrices of finite nuclei with an appropriate treatment of the center-of-mass motion," *Eur. Phys. J.* **A27** (2006) 143–155, arXiv:nucl-th/0602056 [nucl-th].

[37] Z. Zhang and C. M. Ko, "Hypertriton production in relativistic heavy ion collisions," *Phys. Lett.* **B780** (2018) 191–195.

[38] A. Andronic, P. Braun-Munzinger, K. Redlich, and J. Stachel, "Hadron yields, the chemical freeze-out and the QCD phase diagram," *J. Phys. Conf. Ser.* **779** no. 1, (2017) 012012, arXiv:1611.01347 [nucl-th].

[39] K. Blum, K. C. Y. Ng, R. Sato, and M. Takimoto, "Cosmic rays, antihelium, and an old navy spotlight," *Phys. Rev.* **D96** no. 10, (2017) 103021, arXiv:1704.05431 [astro-ph.HE].

[40] **ALICE** Collaboration, B. Abelev *et al.*, "Centrality determination of Pb-Pb collisions at $\sqrt{s_{NN}} = 2.76$ TeV with ALICE," *Phys. Rev.* **C88** no. 4, (2013) 044909, arXiv:1301.4361 [nucl-ex].

[41] **ALICE** Collaboration, K. Aamodt *et al.*, "Two-pion Bose-Einstein correlations in central Pb-Pb collisions at $\sqrt{s_{NN}} = 2.76$ TeV," *Phys. Lett.* **B696** (2011) 328–337, arXiv:1012.4035 [nucl-ex].

[42] **ALICE** Collaboration, J. Adam *et al.*, "Two-pion femtoscopy in p-Pb collisions at $\sqrt{s_{\mathrm{NN}}} = 5.02$ TeV," *Phys. Rev.* **C91** (2015) 034906, arXiv:1502.00559 [nucl-ex].

[43] **ALICE** Collaboration, B. Abelev *et al.*, "Charged kaon femtoscopic correlations in *pp* collisions at $\sqrt{s} = 7$ TeV," *Phys. Rev.* **D87** no. 5, (2013) 052016, arXiv:1212.5958 [hep-ex].

[44] **ALICE** Collaboration, J. Adam *et al.*, "One-dimensional pion, kaon, and proton femtoscopy in Pb-Pb collisions at $\sqrt{s_{\mathrm{NN}}} = 2.76$ TeV," *Phys. Rev.* **C92** no. 5, (2015) 054908, arXiv:1506.07884 [nucl-ex].

[45] M. Petran, J. Letessier, J. Rafelski, and G. Torrieri, "SHARE with CHARM," *Comput. Phys. Commun.* **185** (2014) 2056–2079, arXiv:1310.5108 [hep-ph].

[46] S. Wheaton and J. Cleymans, "THERMUS: A Thermal model package for ROOT," *Comput. Phys. Commun.* **180** (2009) 84–106, arXiv:hep-ph/0407174 [hep-ph].

[47] A. Andronic, P. Braun-Munzinger, and J. Stachel, "Hadron production in central nucleus-nucleus collisions at chemical freeze-out," *Nucl. Phys.* **A772** (2006) 167–199, arXiv:nucl-th/0511071 [nucl-th].

[48] E. Schnedermann, J. Sollfrank, and U. W. Heinz, "Thermal phenomenology of hadrons from 200-A/GeV S+S collisions," *Phys. Rev.* **C48** (1993) 2462–2475, arXiv:nucl-th/9307020 [nucl-th].

[49] **ALICE** Collaboration, B. Abelev *et al.*, "Pion, Kaon, and Proton Production in Central Pb–Pb Collisions at $\sqrt{s_{NN}} = 2.76$ TeV," *Phys. Rev. Lett.* **109** (2012) 252301, arXiv:1208.1974 [hep-ex].

[50] **ALICE** Collaboration, B. B. Abelev *et al.*, "K_S^0 and Λ production in Pb-Pb collisions at $\sqrt{s_{NN}} = 2.76$ TeV," *Phys. Rev. Lett.* **111** (2013) 222301, arXiv:1307.5530 [nucl-ex].

[51] **ALICE** Collaboration, J. Adam *et al.*, "$^3_\Lambda$H and $^3_\Lambda\overline{\mathrm{H}}$ production in Pb-Pb collisions at $\sqrt{s_{\mathrm{NN}}} = 2.76$ TeV," *Phys. Lett.* **B754** (2016) 360–372, arXiv:1506.08453 [nucl-ex].

[52] U. A. Wiedemann and U. W. Heinz *Phys. Rept.* **319** (1999) 145.